

DOI: 10.1002/ ((please add manuscript number))

Article type: Full Paper

## Amorphous Dual-layer Coating: Enabling High Li-ion Conductivity of Non-sintered Garnet-type Solid Electrolyte

*Yuan Gao, Shuyang Sun, Xin Zhang, Yongfeng Liu\*, Jianjiang Hu, Zhenguo Huang, Mingxia Gao, and Hongge Pan*

Y. Gao, S. Y. Sun, Dr. X. Zhang, Prof. Y. F. Liu, Prof. M. X. Gao, Prof. H. G. Pan  
State Key Laboratory of Silicon Materials and School of Materials Science and Engineering,  
Zhejiang University, Hangzhou 310027, China

E-mail: mselyf@zju.edu.cn

Prof. J. J. Hu

School of Chemistry and Chemical Engineering, Yantai University, Yantai 264005, China

Prof. Z. G. Huang

School of Civil & Environmental Engineering, University of Technology Sydney, 81  
Broadway, Ultimo, NSW, 2007, Australia

Keywords: energy storage materials, rechargeable Li batteries, solid state electrolyte, borohydrides, LLZTO

### Abstract:

Garnet-type oxide  $\text{Li}_{6.4}\text{La}_3\text{Zr}_{1.4}\text{Ta}_{0.6}\text{O}_{12}$  (LLZTO) has attracted considerable attention as a highly promising solid state electrolyte. However, its high ionic conductivity is achievable only after high temperature sintering ( $\sim 1200$  °C) to form dense pellets but with detrimental brittleness and poor contact with electrodes. Herein, we demonstrate a novel strategy to achieve high  $\text{Li}^+$  ion conductivity of LLZTO without sintering. This was realized by ball milling LLZTO together with  $\text{LiBH}_4$ , which resulted in a LLZTO composite with unique amorphous dual coating:  $\text{LiBO}_2$  as the inner layer and  $\text{LiBH}_4$  as the outer layer. After cold pressing the LLZTO composite powders under 300 MPa to form electrolyte pellets, a high  $\text{Li}^+$  ion conductivity of  $8.02 \times 10^{-5} \text{ S cm}^{-1}$  was obtained at 30 °C, which is four orders of magnitude higher than that of the non-sintered pristine LLZTO pellets ( $4.17 \times 10^{-9} \text{ S cm}^{-1}$ ). The composite electrolyte displays an ultrahigh  $\text{Li}^+$  transference number of 0.9999 and enables symmetric Li-Li cells to be cycled for 1000 h at 60 °C and 300 h at 30 °C. The significant improvements are attributed to the

continuous ionic conductive network among LLZTO particles facilitated by  $\text{LiBH}_4$  that is chemically compatible with and electrochemically stable relative to Li metal electrode.

## 1. Introduction

The rapid development of electronic devices and electric vehicles raises the demand for batteries with high energy density, long cycling life and better safety.<sup>[1]</sup> All solid-state batteries (ASSBs) have therefore attracted significant attention because solid state electrolytes (SSEs) enhance safety and overall electrochemical performance.<sup>[2]</sup> Several types of compounds have been investigated as SSEs including oxides, sulfides and hydrides.<sup>[3]</sup> Among them, the garnet-type oxide  $\text{Li}_7\text{La}_3\text{Zr}_2\text{O}_{12}$  (LLZO) and its derivatives hold great promise because of their high ionic conductivity and good chemical stability.<sup>[4]</sup> In particular, Ta-doped LLZO ceramic electrolyte (LLZTO) delivers a  $\text{Li}^+$  ion conductivity of  $10^{-4}$  -  $10^{-3}$   $\text{S cm}^{-1}$  at ambient temperature, which is much higher than LLZO and even comparable to traditional liquid electrolytes.<sup>[5]</sup> However, the LLZTO electrolyte does not readily integrate with Li metal anode due to an incompact structure arising from its extremely high Young's modulus (150 GPa) and the poor interface contact between LLZTO and Li metal.<sup>[6]</sup> Dense ceramic pellets need to be prepared by high-pressure compression followed by sintering at high temperatures ( $\sim 1200$  °C),<sup>[7]</sup> which is time consuming and energy intensive. In addition, the sintered ceramic pellets are usually thick and fragile, and difficult for upscaled applications.<sup>[8]</sup>

Considerable efforts have been devoted to improving the applicability of LLZTO by reducing the sintering temperatures and/or blending with polymers. For example, oxides such as  $\text{Li}_3\text{BO}_3$ ,  $\text{SiO}_2$  and  $\text{La}_2\text{Zr}_2\text{O}_7$ , were employed as sintering aids to bridge the grain boundaries and improve densification at lowered sintering temperatures.<sup>[9-11]</sup> An 28% increase in the relative density was achieved for LLZTO after introducing 1 mol%  $\text{SiO}_2$ .<sup>[10]</sup> Similar phenomenon was also observed for LLZTO electrolyte mixed with  $\text{La}_2\text{Zr}_2\text{O}_7$  by promoting the formation of glass-like phases binding LLZTO grains.<sup>[11]</sup> However, high temperature sintering is still necessary for the

preparation of solid electrolyte pellets. LLZTO-polymer composite electrolytes have also been studied by embedding LLZTO powders into polymer matrices, which offer advantages including good processability, lightweight and good contact with electrodes.<sup>[12,13]</sup> However, their Li<sup>+</sup> transference numbers are relatively low (below 0.8) due to the inert polymer matrices, and heating treatment above 150 °C is still needed to melt the polymers to form composite electrolytes.

Recently, surface engineering proves effective to improve the density of electrolyte pellets with reduced interface resistance and enhanced ionic conductivity at lower sintering temperatures.<sup>[7b,14]</sup> Tian et al. fabricated a LLZTO composite electrolyte coated with amorphous Li<sub>3</sub>OCl by melting-quenching at 350 °C.<sup>[14]</sup> The amorphous Li<sub>3</sub>OCl worked as a binder and bridge to fill the voids of LLZTO pellets. In another study, LiCl-coated LLZTO electrolyte pellets exhibited three orders of magnitude higher ionic conductivity than pristine LLZTO, but their preparation involved water or ethanol solutions which needs to be removed before use.<sup>[7b]</sup> So far, no success has been reported in achieving both high ionic conductivity and high Li<sup>+</sup> transference number for LLZTO pellets prepared merely by cold pressing without sintering.

In this work, we report for the first time a scalable method to engineer the surface of LLZTO particles to achieve high ionic conductivity and good electrochemical properties. This was realized simply by ball milling LLZTO with LiBH<sub>4</sub>, leading to the formation of a unique LLZTO composite with dual-layer coatings, i.e., LiBO<sub>2</sub> as the inner and LiBH<sub>4</sub> as the outer layer. After cold pressing under 300 MPa, a SSE of the LLZTO composite with high Li<sup>+</sup> ion conductivity ( $8.02 \times 10^{-5} \text{ S cm}^{-1}$ ) at 30 °C was obtained. An ultrahigh Li<sup>+</sup> transference number of 0.9999 as well as a wide electrochemical window (6 V vs. Li / Li<sup>+</sup>) were achieved. A symmetric Li|LLZTO-4LiBH<sub>4</sub>|Li cell was cycled stably at 60 °C for more than 1000 h and at 30 °C for more than 300 h at 0.15 mA cm<sup>-2</sup>. Our work opens a new possibility to practically apply non-sintered garnet-type LLZTO composite electrolyte for high-performance ASSLBs.

## 2. Results and Discussion

### 2.1 Preparation and characterization of the LLZTO composite electrolyte

The dual amorphous layer-coated LLZTO composite was prepared by ball milling LLZTO and  $\text{LiBH}_4$  on a planetary ball mill (**Figure 1a**).  $\text{H}_2$  was detected in the gas evolved during ball milling by mass spectrometry (MS) analysis (**Figure S1**, Supporting Information), which indicates a reaction between LLZTO and  $\text{LiBH}_4$ . The resultant solid-state products were characterized by X-ray diffraction (XRD), electron paramagnet resonance (EPR), Fourier transform infrared (FTIR) spectroscopy, scanning electron microscopy (SEM), transmission electron microscopy (TEM), energy dispersive X-ray spectroscopy (EDS) and X-ray photoelectron spectroscopy (XPS). **Figure 1b** and **c** show the XRD patterns and FTIR spectra of the milled LLZTO- $x\text{LiBH}_4$  samples. XRD patterns reveal only the cubic phase LLZO (PDF No. 01-080-6143) (**Figure 1b**), whereas no phase related to  $\text{LiBH}_4$  could be indexed, even for the LLZTO-8 $\text{LiBH}_4$  sample, implying that boron-containing species became amorphous. A slight low-angle shift in the XRD peaks of LLZTO with increasing  $\text{LiBH}_4$  amount was observed, especially noticeable for the strongest reflection (4 2 2), indicating an increase in the lattice parameters. The EPR measurement displays a strong signal around 3500 G indicating the presence of oxygen vacancies (**Figure 1c**),<sup>[15]</sup> which was further evidenced by high-resolution XPS spectra (**Figure 1d**) displaying lowered oxidation states of Zr and Ta after ball milling. We therefore believe that in addition to  $\text{LiBO}_2$  and  $\text{H}_2$ , oxygen vacancies were created in the LLZTO structure after reacting with  $\text{LiBH}_4$ , which explains the slightly enlarged lattice parameters.<sup>[1d,16]</sup> The characteristic IR bands of B-H vibration in  $\text{LiBH}_4$  at 2386, 2293, 2226 and  $1127\text{ cm}^{-1}$  were visible,<sup>[17]</sup> especially for samples with high  $\text{LiBH}_4$  contents (**Figure 1e**). In addition, the IR band position at 1442, 879, 763 and  $692\text{ cm}^{-1}$  assignable to B-O vibrations were discernable, pointed to the formation of  $\text{LiBO}_2$ .<sup>[18]</sup> These results indicate that the resultant solid-state products were composed of oxygen-vacancy-rich LLZTO,  $\text{LiBO}_2$  and  $\text{LiBH}_4$ . As a strong

reducing agent,  $\text{LiBH}_4$  reacted with LLZTO, initiated by energetic collisions between milling balls, forming  $\text{LiBO}_2$  and oxygen vacancies in LLZTO along with  $\text{H}_2$ .

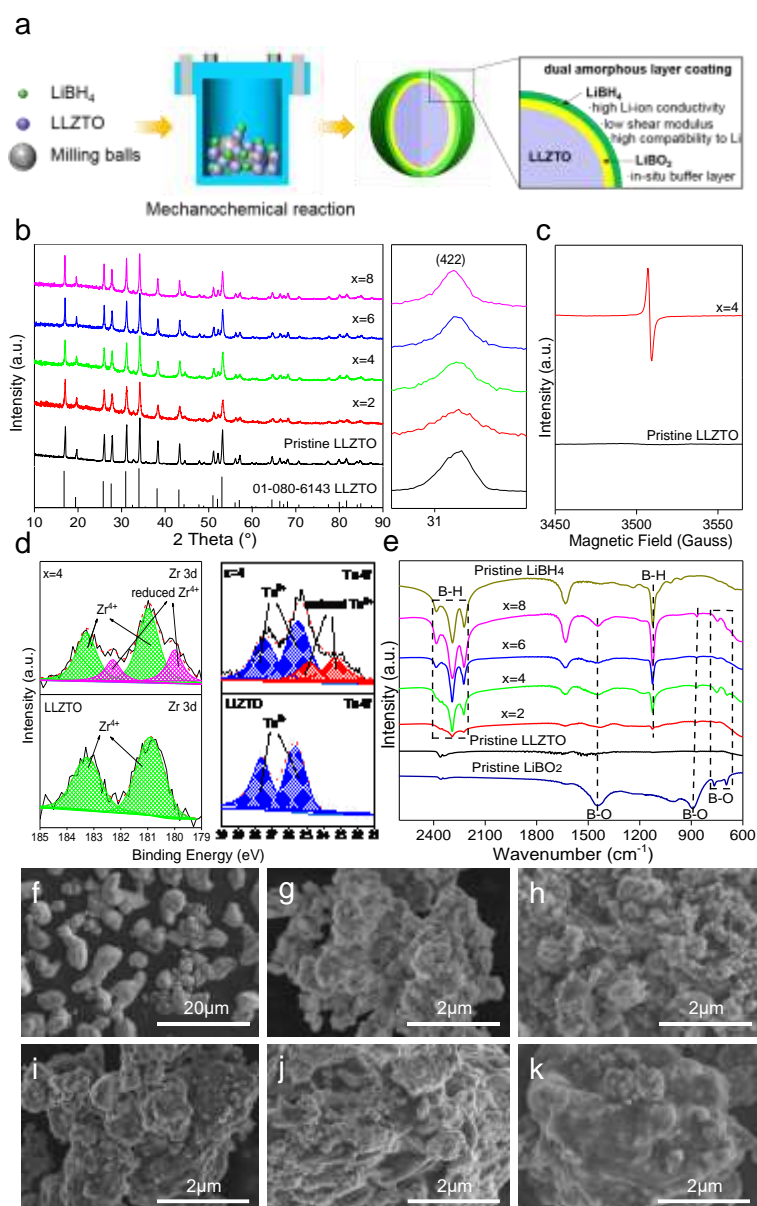


**Figure 1.** a) Schematic of the preparation of  $\text{LiBH}_4$ -modified LLZTO. b) XRD patterns, c) EPR spectra, d) high resolution XPS spectra of Zr 3d and Ta 4f and e) FTIR spectra of the milled LLZTO- $x\text{LiBH}_4$  samples. SEM images of f) LLZTO raw material and the milled LLZTO- $x\text{LiBH}_4$  samples for g)  $x = 0$ , h)  $x = 2$ , i)  $x = 4$ , j)  $x = 6$  and k)  $x = 8$ .

**Figure 1f-k** present the SEM images of pristine LLZTO and as-milled LLZTO- $x\text{LiBH}_4$  samples. Pristine LLZTO particles appear irregular in shape and the particle sizes range from 5 to 10  $\mu\text{m}$  (**Figure 1f**). Ball milling effectively pulverized the particles which became smaller

than 5  $\mu\text{m}$  in size (**Figure 1g**). The introduction of  $\text{LiBH}_4$  during ball milling leads to the aggregation and adhesion of particles (**Figure 1h-k**), which even exhibit encapsulation-like morphology for the sample at  $x = 8$ . This is possibly due to the low Young's modulus of  $\text{LiBH}_4$  and newly formed  $\text{LiBO}_2$  enabling coatings around hard LLZTO particles, which would improve the processability and formability of LLZTO under cold-pressing treatment.

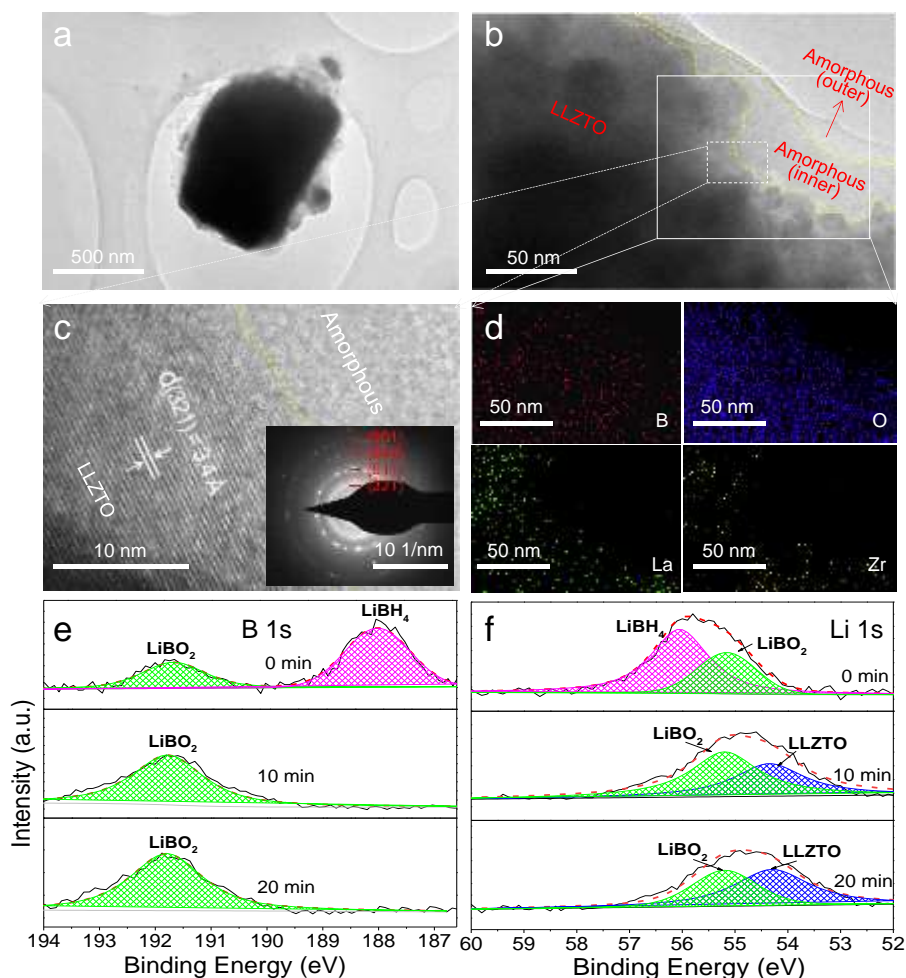


**Figure 2.** a, b) TEM, c) HRTEM images and d) the corresponding EDS mapping images of the as-milled LLZTO-4LiBH<sub>4</sub> sample. The inset of c) is the SAED pattern. High resolution XPS spectra of e) B 1s and f) Li 1s of the LLZTO-4LiBH<sub>4</sub> sample before and after sputtering.

Further TEM observations reveal dual coatings on LLZTO particles for the LiBH<sub>4</sub>-containing sample (**Figure 2a and b**). The high-resolution TEM (HRTEM) image (**Figure 2c**) presents amorphous coating and fringes with interplanar spacings of 0.34 nm for the core corresponding

to (321) crystal plane of LLZTO. EDS mapping indicates that element B concentrates on the surface while La and Zr are in the inner core (**Figure 2d**). EDS point analyses also prove that B dominates points 1 and 2 at the surface while the relative contents of La, Zr, Ta and O are significantly higher for point 3 in the inner (**Figure S2**, Supporting Information). This indicates that after ball milling the LLZTO particles are covered by B-containing amorphous layers.

**Figure 2e** and **f** show the XPS depth profile of element B and Li in LLZTO-4LiBH<sub>4</sub> (the sample with the highest SSE performance, discussion in the following sections) before and after sputtering. The high-resolution B 1s XPS spectrum (**Figure 2e**) exhibits the typical binding energy of B(-H) in LiBH<sub>4</sub> at 187.8 eV before sputtering.<sup>[19]</sup> After sputtering for 10 min and 20 min, a new B 1s XPS peak corresponding to B(-O) in LiBO<sub>2</sub> at 191.7 eV was observed along with the disappearance of LiBH<sub>4</sub>.<sup>[20]</sup> For the high-resolution Li 1s XPS spectra of the milled sample (**Figure 2f**), there are two Li 1s peaks with the stronger one at 56.2 eV attributed to LiBH<sub>4</sub> and the weaker one at 55.2 eV attributed to LiBO<sub>2</sub>. After 10 minutes of sputtering, the Li 1s peak belonging to LLZTO at 54.5 eV appeared,<sup>[21]</sup> and that of LiBH<sub>4</sub> disappeared. Further increasing the sputtering time to 20 min, the relative intensity of Li 1s peak of LLZTO increased, while that of LiBO<sub>2</sub> weakened. This clearly demonstrates that the amorphous coating is a dual-layer structure consisting of LiBH<sub>4</sub> as the outer and LiBO<sub>2</sub> as the inner layer. Here, the *in-situ* formation of LiBO<sub>2</sub> in immediate contact with LLZTO serves as a buffer layer to prevent further reaction between LiBH<sub>4</sub> and LLZTO during ball milling. This is reasonably explained by the fact that the content of newly formed LiBO<sub>2</sub> increased gradually with ball milling time and then stabilized when approaching 12 h (**Figure S3**, Supporting Information). The shear moduli of LiBH<sub>4</sub> (~5 GPa) and LiBO<sub>2</sub> (30 GPa) are much lower than that of LLZTO (60 GPa),<sup>[6b,22]</sup> which facilitates the formation of compact coating around LLZTO particles. The amorphous coatings therefore improve the processability of LLZTO particles to obtain compact SSE pellets. Moreover, it should note that LiBH<sub>4</sub> is a fast lithium ion conductor and is electrochemically stable to Li metal.<sup>[23,24]</sup>

## 2.2 Ionic conductivity of the LLZTO composite electrolyte

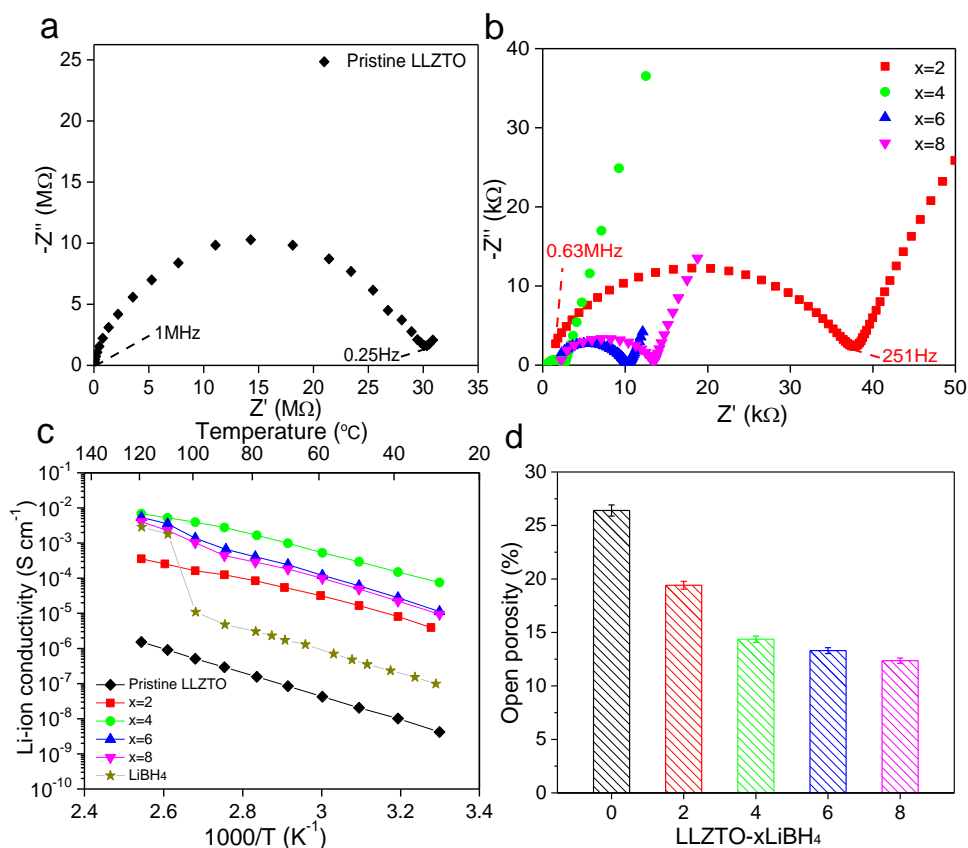


**Figure 3.** a, b) Nyquist curves, c) Arrhenius plots and d) open porosity of the LLZTO- $x$ LiBH $_4$  pellets.

To determine the Li<sup>+</sup> ion conductivity, the as-milled LLZTO- $x$ LiBH $_4$  composite was cold pressed into pellets at room temperature and then directly subjected to EIS examination. All the electrochemical impedance spectra (EIS) collected at 30 °C exhibit similar shape composing of a semicircle and a straight line (**Figure 3a** and **b**), where the semicircle diameter is correlated to resistance associated with grain boundary and pores inside the solid electrolyte ( $R_{g+p}$ ), and the straight line at low frequency region is related to resistance to ion transfer.<sup>[25]</sup> Here, the  $R_{g+p}$  value of the LLZTO-4LiBH $_4$  sample was determined to be only 2.5 k $\Omega$ , in contrast to 30.5 M $\Omega$  for the pristine LLZTO pellet, which means a remarkable improvement in ionic conductivity of LLZTO after ball milled with LiBH $_4$ . Moreover, the 12 h ball milled LLZTO-4LiBH $_4$  sample delivered the smallest  $R_{g+p}$  value in the present study (**Figure S4**, Supporting Information). This

ball milling duration seems to generate an optimal combination of reduced LLZTO particle sizes, sufficient LiBH<sub>4</sub> surface coating and LiBO<sub>2</sub> inner layer.

The ionic conductivity ( $\sigma_{\text{Li}^+}$ ) was calculated according to the following equation and listed in **Table S1** (Supporting Information).

$$\sigma_{\text{Li}^+} = \frac{d}{SR_t} \quad (1)$$

where  $S$  is the pellet area,  $d$  the thickness and  $R_t$  the bulk resistance of the electrolyte pellet. As shown in **Table S1** (Supporting Information), the ionic conductivity of the LLZTO- $x$ LiBH<sub>4</sub> composite first increases and then decreases with LiBH<sub>4</sub> content. The highest Li<sup>+</sup> ion conductivity was obtained for the LLZTO-4LiBH<sub>4</sub> sample, which is  $8.02 \times 10^{-5} \text{ S cm}^{-1}$  at 30 °C. This value is about four orders of magnitude higher than that of pristine LLZTO ( $4.17 \times 10^{-9} \text{ S cm}^{-1}$ ) and even approaching to some LLZTO-based SSEs prepared by high-temperature sintering.<sup>[26]</sup>

Temperature dependence of the ionic conductivities of LLZTO- $x$ LiBH<sub>4</sub> composites was plotted in **Figure 3c**. There is a good linear relationship between the logarithms of ionic conductivity with the reciprocal of temperatures. The activation energy can be deduced by fitting the plots shown in **Figure 3c** at 30-80 °C using the Arrhenius equation.

$$\sigma_{\text{Li}^+} = \left(\frac{A}{T}\right) \exp\left(-\frac{E_a}{kT}\right) \quad (2)$$

in which  $A$  is the pre-exponential factor,  $E_a$  is the activation energy,  $k$  is the Boltzmann constant and  $T$  is the temperature in Kelvin. As shown in **Table S1** (Supporting Information), the  $E_a$  value of the sample at  $x = 4$  was calculated to be 0.60 eV, which is apparently lower than that of pristine LLZTO (0.70 eV), suggesting a lower energy barrier for Li<sup>+</sup> ion movement in the LiBH<sub>4</sub>-modified samples. It should be noted that for samples with  $x > 4$ , the temperature dependence of the ionic conductivities becomes very similar to that of LiBH<sub>4</sub> at elevated temperature, indicating that LiBH<sub>4</sub> dominates the electrochemical behavior.

Unlike previous reports, we obtained high  $\text{Li}^+$  ion conductivity for the LLZTO- $x\text{LiBH}_4$  SSE pellets prepared simply by cold pressing without further treatment. To understand the underlying mechanism, open porosity of the SSE pellets was measured. As shown in **Figure 3d**, the presence of  $\text{LiBH}_4$  effectively reduces the open porosity from 26.4% for pristine LLZTO to 14.4% for the  $x = 4$  composite and further to 12.3% for the  $x = 8$  composite, which is also evidenced by SEM observation (**Figure 4a** and **b**). Cavities are clearly visible for pristine LLZTO due to its poor deformability caused by high stiffness,<sup>[6b]</sup> which leads to point contacts instead of face contacts and therefore restricted  $\text{Li}^+$  ion mobility (**Figure 4c**). With the presence of  $\text{LiBH}_4$ , the pellet becomes dense with much reduced cavities. This is likely due to the lower shear moduli of  $\text{LiBH}_4$  (~5 GPa) and  $\text{LiBO}_2$  (30 GPa) in comparison with LLZTO (60 GPa),<sup>[6b,22]</sup> which improve the ductility of particles. Thus,  $\text{LiBH}_4$  and newly formed  $\text{LiBO}_2$  are believed to work as a filler and binder to densify the pellets, where more face contacts are established, facilitating  $\text{Li}^+$  ion transport between particles (**Figure 4d**). However, too much  $\text{LiBH}_4$  resulted in a thicker coating, which slows down the  $\text{Li}^+$  ion transport between particles,<sup>[27]</sup> as schematically illustrated in **Figure 4e**. This explains that the optimal  $\text{Li}^+$  ion conductivity appears at  $x = 4$ .

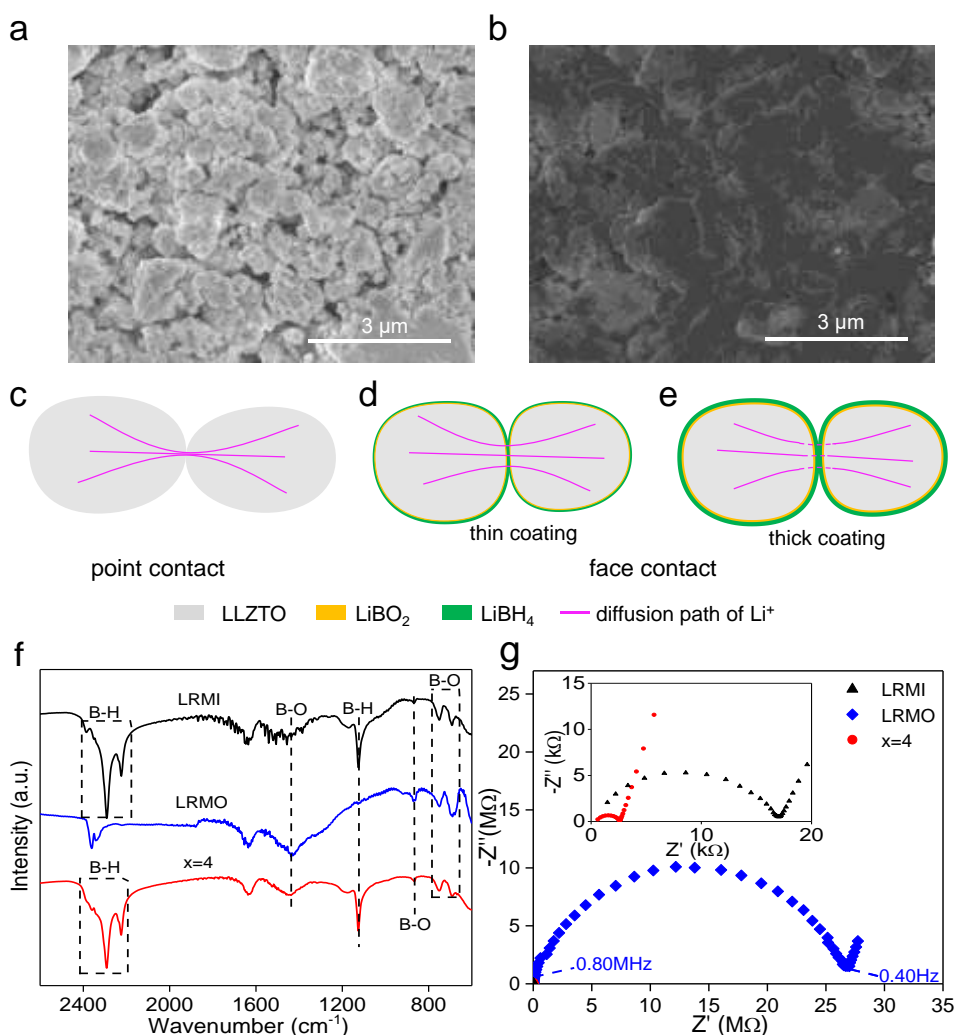


**Figure 4.** SEM images of pellets of a) pristine LLZTO and b) LLZTO-4LiBH<sub>4</sub>. Schematic illustration of contact and the Li<sup>+</sup> diffusion path between particles in the pellets of c) pristine LLZTO sample, with d) low and e) high LiBH<sub>4</sub> content. f) FTIR spectra and g) Nyquist plots of the LLZTO-4LiBH<sub>4</sub> samples with LiBH<sub>4</sub> removed (LRMO) and reintroduced (LRMI).

To understand the roles played by LiBH<sub>4</sub> and LiBO<sub>2</sub>, we removed LiBH<sub>4</sub> on the surface layer of the as-prepared LLZTO composite using diethyl ether in a glove box. The resultant sample was named as LRMO. After such treatment, the characteristic absorbances of B-H bond in LiBH<sub>4</sub> at 2386, 2293, 2226 and 1127 cm<sup>-1</sup> became absent in the FTIR spectra while those of B-O bond in LiBO<sub>2</sub> at 1442, 879, 763 and 692 cm<sup>-1</sup> were still visible (**Figure 4f**), which confirms the removal of LiBH<sub>4</sub>. An increased open porosity of 24.95% was observed in the pellet

obtained by cold pressing LRMO under 300 MPa (**Figure S5**, Supporting Information), very close to that of pristine LLZTO, consequently inducing a great decrease in the Li<sup>+</sup> ion conductivity ( $\sim 10^{-9}$  S cm<sup>-1</sup>) (**Figure 4g**). Therefore it is LiBH<sub>4</sub> rather than LiBO<sub>2</sub> playing the role in filling the gap and facilitating ion transfer in the LLZTO-*x*LiBH<sub>4</sub> pellets. This conjecture was further confirmed by the fact that the open porosity was reduced (**Figure S5**, Supporting Information) and the Li<sup>+</sup> ion conductivity was recovered again to a value comparable to the *x* = 4 sample after remixing with a certain amount of LiBH<sub>4</sub> (denoted as LRMI), and the bulk resistance ( $R_{g+p}$ ) was largely reduced from approximately 27 MΩ to 17 kΩ (**Figure 4g**). In addition, no appreciable change in the bulk resistance was observed for a LLZTO-LiBO<sub>2</sub> composite which was obtained by ball milling LiBO<sub>2</sub> with LLZTO (**Figure S6**, Supporting Information). Here, the LRMO sample displays slightly reduced bulk resistance (27 MΩ) compared with the LLZTO-LiBO<sub>2</sub> composite (29 MΩ). This difference could be attributed to the presence of oxygen vacancies since the LRMO sample consists of the oxygen-vacancy-rich LLZTO apart from LiBO<sub>2</sub> as mentioned above. However, such improvement is negligible compared with the enhancement caused by the presence of LiBH<sub>4</sub>. As for LiBO<sub>2</sub>, its *in-situ* formation prevents further reaction between LiBH<sub>4</sub> and LLZTO during ball milling, consequently resulting in the formation of the LiBH<sub>4</sub> outer layer. In addition, the presence of the LiBO<sub>2</sub> inner layer is also favorable for cycling for Li symmetric cells by avoiding the direct contact between LiBH<sub>4</sub> and LLZTO as discussed later.

The electronic conductivity of the LLZTO-4LiBH<sub>4</sub> composite was further measured on a SUS|SSE|SUS blocking cell by direct current (DC) polarization technique. **Figure 5a** shows the time dependence of current after applying step voltage of 100 mV at 30 °C. The discharge current first rapidly decreased and then stabilized with time. The electronic conductivity ( $\sigma_e$ ) was calculated to be  $4.07 \times 10^{-9}$  S cm<sup>-1</sup> using the following equation.

$$\sigma_e = \frac{I_0 d}{U_0 S} \quad (3)$$

where  $I_0$  is the steady current,  $U_0$  is the applied voltage,  $d$  is the thickness and  $S$  is the area of the SSE pellet. This value is lower than those reported previously ( $10^{-8}$  -  $10^{-7}$  S cm $^{-1}$ ) for the sintered LLZTO electrolyte pellets,<sup>[28]</sup> and nearly four orders of magnitude lower than that of Li $^{+}$  ion conductivity. The Li $^{+}$  transference number was determined to be higher than 0.9999, which has been rarely reported. As a result, the electronic conduction in the LiBH $_4$ -modified SSE sample is negligible, which would suppress the growth of Li dendrite and therefore enhance cycling performance.<sup>[28b]</sup>

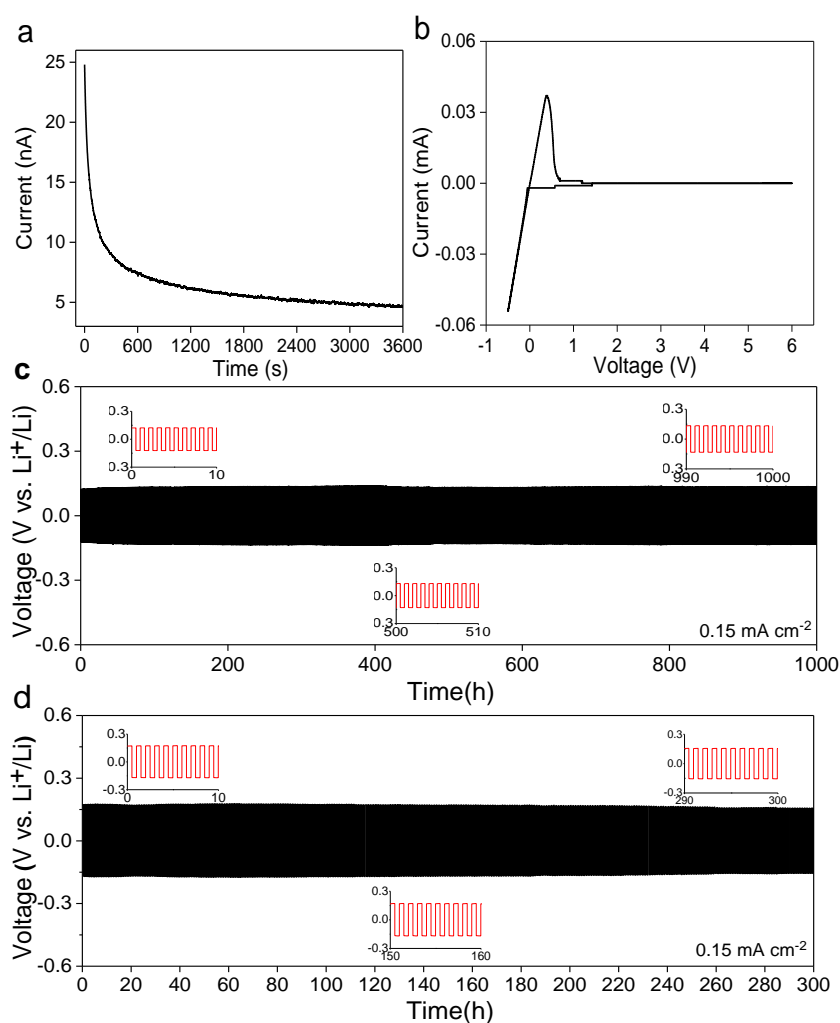


**Figure 5.** a) DC polarization curve, b) CV curve, and galvanostatic cycling curves at c) 60 °C and d) 30 °C of the Li|LLZTO-4LiBH $_4$ |Li cells. The insets show the detailed voltage plateau of Li stripping/plating at selected cycles.

### 2.3 Electrochemical performance of the LLZTO composite electrolyte

**Figure 5b** shows the cyclic voltammetry (CV) curve of the SUS|SSE|Li measured at a scan rate of  $0.1 \text{ mV s}^{-1}$ . It is clear that no additional redox peaks were observed beside the Li plating-stripping peaks between the voltage range of  $-0.5 \text{ V}$  and  $6 \text{ V}$ , indicating that the  $\text{LiBH}_4$ -modified LLZTO electrolyte was electrochemically stable up to  $6 \text{ V}$  (vs.  $\text{Li}^+/\text{Li}$ ). It was reported that  $\text{LiBH}_4$  is chemically compatible and electrochemically stable to Li metal with an electrochemical window above  $5 \text{ V}$  (vs.  $\text{Li}^+/\text{Li}$ ).<sup>[23,24]</sup> The SSE obtained here can therefore be applied to high-voltage solid-state Li and/or Li-ion batteries.

**Figure 5c** and **d** show the galvanostatic cycling curve of a  $\text{Li}|\text{LLZTO-4LiBH}_4|\text{Li}$  cell at a constant current density of  $0.15 \text{ mA cm}^{-2}$  at  $60 \text{ }^\circ\text{C}$  and  $30 \text{ }^\circ\text{C}$ , respectively. Although a  $\text{Li}|\text{LLZTO}|\text{Li}$  cell was also assembled and measured under identical conditions for comparison, it nevertheless could not work properly due to the extremely high overpotential ( $> 5 \text{ V}$  even at  $0.00015 \text{ mA cm}^{-2}$ ) caused by the extremely low conductivity of the cold-pressed LLZTO pellets. In contrast, the  $\text{Li}|\text{LLZTO-4LiBH}_4|\text{Li}$  cell delivered stable and good long-term cycling performance. At  $60 \text{ }^\circ\text{C}$ , no obvious voltage fluctuations were observed with a low overpotential of  $130 \text{ mV}$  even after cycling for more than  $1000 \text{ h}$ . For cycling at  $30 \text{ }^\circ\text{C}$ , the overpotential slightly increased to  $150 \text{ mV}$  and the voltage remained still stable after  $300 \text{ h}$  of cycling. This remarkable cycling performance can be attributed to three factors including the stable surface contact among particles due to the filling of  $\text{LiBH}_4$  in the pellets, the effective separation between  $\text{LiBH}_4$  and LLZTO to prevent their reaction and the extremely low electronic conductivity that effectively suppresses the growth of Li dendrite.<sup>[28b]</sup> As shown in the cross-section SEM images (**Figure 6a** and **b**), the LLZTO-4LiBH<sub>4</sub> composite pellet displays a compact structure, while there are a large number of voids for the pristine LLZTO pellet cold pressing under  $300 \text{ MPa}$ . Even after cycling for  $1000 \text{ h}$  at  $60 \text{ }^\circ\text{C}$ , the  $\text{LiBH}_4$ -modified electrolyte pellet maintains good compactness (**Figure 6c**). In addition, shortening ball milling time induced a poor cycling stability for  $\text{LiBH}_4$ -modified LLZTO (**Figure S7**, Supporting

Information), which can be attributed to the insufficient  $\text{LiBO}_2$  inner layer coating as characterized by high-resolution B 1s XPS spectra (**Figure S3**, Supporting Information).

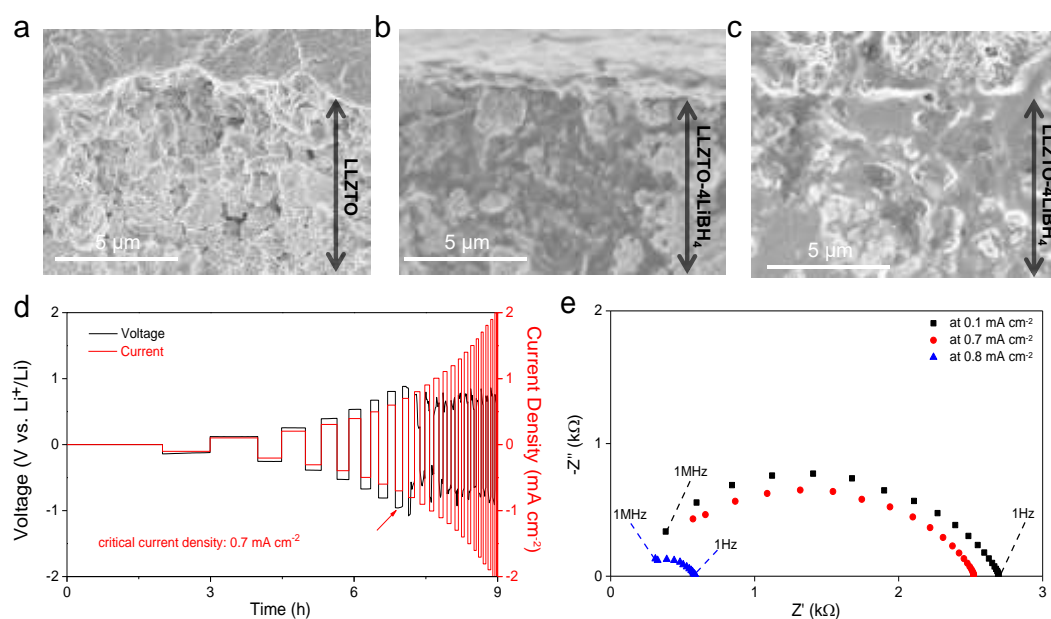


**Figure 6.** Cross-section SEM images of a) the cold-pressed LLZTO and the LLZTO-4LiBH<sub>4</sub> pellet b) before and c) after cycling. d) Stepped current density galvanostatic cycling for the Li|LLZTO-4LiBH<sub>4</sub>|Li symmetric cell at 30 °C. e) EIS spectra of the Li|LLZTO-4LiBH<sub>4</sub>|Li cell after charging/discharging at different current densities during CCD measurement.

**Figure 6d** presents the cycling curves of Li|LLZTO-4LiBH<sub>4</sub>|Li at step-wise current densities. The critical current density (CCD) for Li dendrite formation was determined to be  $0.7 \text{ mA cm}^{-2}$ , which is more than twice the typical garnet-type solid electrolytes ( $<0.3 \text{ mA cm}^{-2}$ ).<sup>[7]</sup> Once the current density was increased over  $0.7 \text{ mA cm}^{-2}$ , the voltage displayed apparent fluctuations because of the occurrence of local short circuit, as confirmed by EIS measurement (**Figure 6e**). The impedance semicircle remains nearly unchanged while the current density increased from 0.1 to  $0.7 \text{ mA cm}^{-2}$ . A dramatic reduction in the semicircle diameter was observed when operating at  $0.8 \text{ mA cm}^{-2}$ , indicating a severely decreased resistance due to a local short circuit.<sup>[29]</sup>

## 2.4 Full cell performance of the LLZTO composite electrolyte

To test the compatibility of  $\text{LiBH}_4$ -modified LLZTO composite electrolyte with cathode materials, a full cell of  $\text{LiCoO}_2|\text{LLZTO-4LiBH}_4|\text{Li}$  was constructed and evaluated. The cathode was fabricated by mixing commercial  $\text{LiCoO}_2$  with SSE at a weight ratio of 7:3 and then uniformly spread over the SSE pellet that is prepared by cold pressing. The charge/discharge curves and the cycling stability are shown in **Figure 7**. The  $\text{LiCoO}_2|\text{LLZTO-4LiBH}_4|\text{Li}$  cell displays a typical high-voltage plateau for charge/discharge (**Figure 7a**). The specific capacity was measured to be  $106.5 \text{ mAh g}^{-1}$  at a current density of  $130 \text{ mA g}^{-1}$  for the first cycle with a coulombic efficiency of 85%. The coulombic efficiency increased to 91.5% at the second cycle and further to 95% after 21 cycles. The specific capacity stabilized at  $96 \text{ mAh g}^{-1}$  after 21 cycles, which corresponds to  $\sim 91\%$  of capacity retention, representing a considerable cycling stability. The  $\text{LiCoO}_2|\text{LLZTO-4LiBH}_4|\text{Li}$  full cell was able to power a yellow LED light array as shown in the inset of **Figure 7b**. This preliminary result indicates that  $\text{LiBH}_4$ -modified LLZTO is a promising electrolyte material for ASSLBs. Further investigations to improve the overall properties of ASSLBs using different cathode materials are in progress in our laboratory.

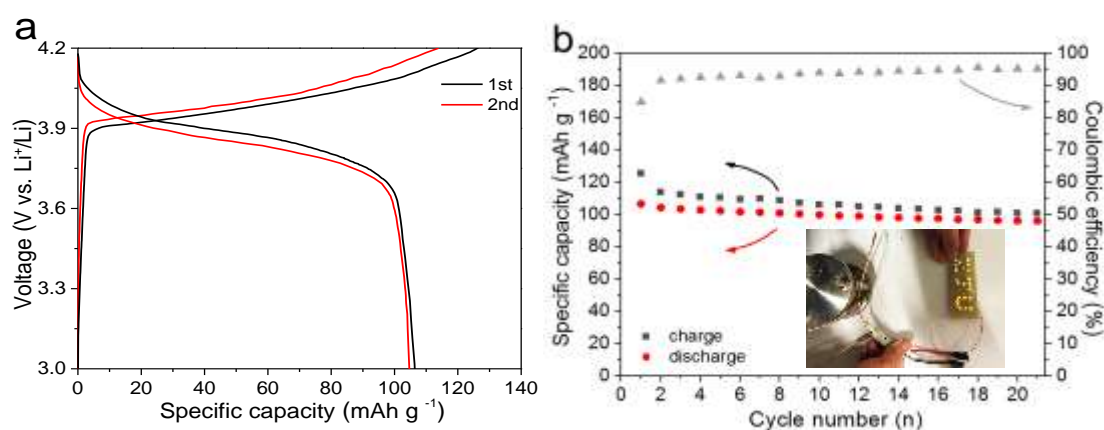


**Figure 7.** a) Charge/discharge profiles and b) cycling performance of a  $\text{LiCoO}_2|\text{LLZTO-4LiBH}_4|\text{Li}$  full cell. The inset displays a digital photograph of LED array powered by the full cell.

### 3. Conclusion

We successfully developed a facile strategy to effectively improve the Li-ion conductivity of LLZTO based solid-state electrolyte. By ball milling LLZTO together with LiBH<sub>4</sub>, we successfully prepared a LLZTO composite featuring dual amorphous coating with LiBO<sub>2</sub> and LiBH<sub>4</sub> as the inner and outer layer, respectively. The amorphous coating results in much enhanced contact among particles by playing the roles of filler, binder and bridge. For SSE pellets obtained by a simple cold pressing process, the open porosity of LiBH<sub>4</sub>-modified LLZTO is less than 50 % of the value for pristine LLZTO. For the LiBH<sub>4</sub>-modified LLZTO pellets, its Li<sup>+</sup> ion conductivity was measured to be  $8.02 \times 10^{-5} \text{ S cm}^{-1}$  at 30 °C, more than four orders of magnitude higher than that of pristine LLZTO ( $4.17 \times 10^{-9} \text{ S cm}^{-1}$ ). The pellet also has extremely low electronic conductivity, which would suppress the formation of Li dendrite. Li<sup>+</sup> transference number was determined to be 0.9999, further confirming the exceptionally high Li<sup>+</sup> ion mobility that has been rarely reported. A symmetric Li cell can be cycled for more than 300 h at 0.15 mA cm<sup>-2</sup> at 30 °C. The LiCoO<sub>2</sub>|LLZTO-4LiBH<sub>4</sub>|Li full cell exhibits a considerable cycling stability with around 100 mAh g<sup>-1</sup> of capacity, demonstrating great potential of non-sintered LLZTO electrolyte for applications in ASSLBs. With its simplicity in fabrication, this approach can be adopted to improve other oxide-based SSEs. For example, various metal (M=Li, Na, K, Mg) borohydrides can be used to modify different oxide-based SSEs for all solid-state batteries (Li/Na/K/Mg based, for instance).

### 4. Experimental Section

*Materials Synthesis.* LLZTO (99.99%) and LiBH<sub>4</sub> (95%) were purchased from MTI and Acros, respectively. Samples of LLZTO composite with LiBH<sub>4</sub> were prepared by ball milling mixtures of LLZTO-*x*LiBH<sub>4</sub> (*x* = 0, 2, 4, 6 and 8, molar ratio). Ball milling was performed on a planetary ball mill (QM-3SP4, Nanjing) at 300 rpm for 12 h. Approximately 1 g of powders were loaded into a milling jar inside an Ar-filled glove box (MBRAUN, Germany). The ball-to-sample

weight ratio was kept at 100:1.

*Characterization.* XRD analysis was performed on a MiniFlex 600 XRD unit (Rigaku, Japan) using Cu K $\alpha$  radiation ( $\lambda = 0.154056$  nm) at 40 kV and 15 mA. The  $2\theta$  angle was from 10 to 90° with a 0.02° increment. FTIR spectra were recorded with a Bruker Tensor 27 unit (Germany). The sample was mixed with dry KBr powders at a weight ratio of 1:300, and then cold pressed into a pellet for measurement. Microstructure and morphology were characterized using a SU8010 SEM operating at 3 kV and a FEI Tecnai G2 F20 S-TWIN TEM operating at 200 kV coupled with an EDS. XPS analyses were conducted on an ESCALAB 250 Xi spectrometer with Al K $\alpha$  X-ray source ( $\lambda = 0.83401$  nm) under a base pressure of  $5 \times 10^{-10}$  Torr. The powder sample was first cold pressed into a pellet inside an argon-filled glove box and then mounted on a sample holder which was transferred using a special container from the glove box to the XPS facility to avoid air exposure. Ar ion sputtering was used for depth profile analysis. EPR spectra were obtained at room temperature using a Bruker A300 EPR spectrometer. The open porosity of SSE pellets was measured in n-heptane medium (Sinopharms). The test pellets were outgassed in a suction flask by vacuuming before immersion into n-heptane.

*Electrochemical Measurements.* For the test cells, stainless steel (SUS) or Li metal electrodes were used to sandwich the SSE, and the assembly was kept in a polyether ether ketone (PEEK) cylinder.<sup>[30]</sup> The LLZO- $x$ LiBH $_4$  SSEs were cold pressed to pellets with 10 mm in diameter and 1-2 mm in thickness. The ionic conductivity of the SSEs was determined by EIS using an Ivium Vertex electrochemical workstation (the Netherlands) in the frequency range of 1 MHz - 1 Hz. DC polarization was conducted by applying a constant voltage of 100 mV for 3600 s. The electrochemical window was examined by performing CV on SUS|SSE|Li cells from -0.5 V to 6 V at a scan rate of 0.1 mV s $^{-1}$ . The galvanostatic plating-stripping cycling was tested on Li|SSE|Li symmetric cells using Neware battery test systems (CT-3008W-5V20A-S4, Shenzhen, China). CCD was determined by cycling at elevated current densities. The LiCoO $_2$ |LLZO-4LiBH $_4$ |Li full cells were assembled and tested from 3.0 to 4.2 V.

Approximately 10 mg of cathode powder was prepared by mixing LiCoO<sub>2</sub> with SSE at a weight ratio of 7:3.

### Supporting Information

Supporting Information is available from the Wiley Online Library or from the author.

### Acknowledgements

We gratefully acknowledge the financial support from the National Natural Science Foundation of China (52071285 and 51831009) and the National Youth Top-Notch Talent Support Program. Z.H. is the recipient of an Australian Research Council Future Fellowship (project number FT190100658).

Received: ((will be filled in by the editorial staff))

Revised: ((will be filled in by the editorial staff))

Published online: ((will be filled in by the editorial staff))

### References

- [1] a) J. M. Tarascon, M. Armand, *Nature*, **2001**, *414*, 359-367; b) S. Chu, A. Majumdar, *Nature* **2012**, *488*, 294-303; c) Y. Cao, M. Li, J. Lu, J. Liu, K. Amine, *Nat. Nanotechnol.* **2019**, *14*, 200-207; d) Y. Yang, X. Qu, X. Zhang, Y. Liu, J. Hu, J. Chen, M. Gao, H. Pan, *Adv. Mater.* **2020**, *32*, 1908285.
- [2] a) Y. S. Hu, *Nat. Energy* **2016**, *1*, 16042; b) E. Quartarone, P. Mustarelli, *Chem. Soc. Rev.* **2011**, *40*, 2525-2540; c) J. Betz, G. Bieker, P. Meister, T. Placke, M. Winter, R. Schmich, *Adv. Energy Mater.* **2019**, *9*, 1803170; d) F. Han, J. Yue, C. Chen, N. Zhao, X. Fan, Z. Ma, T. Gao, F. Wang, X. Guo, C. Wang, *Joule* **2018**, *2*, 497-508.
- [3] a) K. Fu, Y. Gong, G. T. Hitz, D. W. McOwen, Y. Li, S. Xu, Y. Wen, L. Zhang, C. Wang, G. Pastel, J. Dai, B. Liu, H. Xie, Y. Yao, E. D. Wachsman, L. Hu, *Energy Environ. Sci.* **2017**, *10*, 1568-1575; b) A. Manthiram, X. Yu, S. Wang, *Nat. Rev. Mater.* **2017**, *2*, 16103; c) J. Cuan, Y. Zhou, T. Zhou, S. Ling, K. Rui, Z. Guo, H. Liu, X. Yu, *Adv. Mater.* **2019**, *31*, 1803533; d) X. Han, Y. Gong, K. Fu, X. He, G. T. Hitz, J. Dai, A. Pearse, B. Liu, H. Wang, G. Rubloff, Y. Mo, V. Thangadurai, E. D. Wachsman, L. Hu, *Nat. Mater.* **2017**, *16*,

- 572-580; e) Z. Huang, S. Wang, R. D. Dewhurst, N. V. Ignat'ev, M. Finze, H. Braunschweig, *Angew. Chem. Int. Ed.*, **2020**, *59*, 8800 – 8816.
- [4] a) C. Wang, K. Fu, S. P. Kammampata, D. W. McOwen, A. J. Samson, L. Zhang, G. T. Hitz, A. M. Nolan, E. D. Wachsman, Y. Mo, V. Thangadurai, L. Hu, *Chem. Rev.*, **2020**, *120*, 4257-4300; b) L. Xu, J. Li, W. Deng, H. Shuai, S. Li, Z. Xu, J. Li, H. Hou, H. Peng, G. Zou, X. Ji, *Adv. Energy Mater.* **2020**, 2000648; c) N. Zhao, W. Khokhar, Z. Bi, C. Shi, X. Guo, L. Z. Fan, C. W. Nan, *Joule* **2019**, *3*, 1190-1199; d) W. L. Huang, N. Zhao, Z. J. Bi, C. Shi, X. X. Guo, L. Z. Fan, C. W. Nan, *Mater. Today Nano*, **2020**, *10*, 100075.
- [5] a) Y. Zhong, Y. Xie, S. Hwang, Q. Wang, J. J. Cha, D. Su, H. Wang, *Angew. Chem. Int. Ed.* **2020**, *59*, 14003-14008; b) Y. Li, J. T. Han, C. A. Wang, H. Xie, J. B. Goodenough, *J. Mater. Chem.* **2012**, *22*, 15357-15361; c) Y. Chen, E. Rangasamy, C. D. Lang, K. An, *Chem. Mater.* **2015**, *27*, 5491-5494.
- [6] a) Y. Kato, S. Hori, T. Saito, K. Suzuki, M. Hirayama, A. Mitsui, M. Yonemura, H. Iba, R. Kanno, *Nat. Energy*, 2016, *1*, 16030; b) S. Yu, R. D. Schmidt, R. Garcia-Mendez, E. Herbert, N. J. Dudney, J. B. Wolfenstine, J. Sakamoto, D. J. Siegel, *Chem. Mater.* **2016**, *28*, 197-206. c) Y. Lu, X. Huang, Y. Ruan, Q. Wang, R. Kun, J. Yang, Z. Wen, *J. Mater. Chem. A* **2018**, *6*, 18853-18858; d) W. Feng, X. Dong, X. Zhang, Z. Lai, P. Li, C. Wang, Y. Wang, Y. Xia, *Angew. Chem. Int. Ed.* **2020**, *59*, 5346-5349.
- [7] a) R. Chen, Q. Li, X. Yu, L. Chen, H. Li, *Chem. Rev.* **2020**, *120*, 6820–6877; b) Z. Zhang, L. Zhang, C. Yu, X. Yan, B. Xu, L. M. Wang, *Electrochem. Acta*, **2018**, *289*, 254-263.
- [8] a) M. Dirican, C. Yan, P. Zhu, X. Zhang, *Mater. Sci. Eng. R* **2019**, *136*, 27–46; b) W. Li, C. Sun, J. Jin, Y. Li, C. Chen, Z. Wen, *J. Mater. Chem. A* **2019**, *7*, 27304-27312.
- [9] H. Xie, C. Li, W. H. Kan, M. Avdeev, C. Zhu, Z. Zhao, X. Chu, D. Mu, F. Wu, *J. Mater. Chem. A* **2019**, *7*, 20633-20639.
- [10] S. Zhang, H. Zhao, J. Wang, T. Xu, K. Zhang, Z. Du, *Chem. Eng. J.* **2020**, *393*, 124797.
- [11] X. Huang, C. Shen, K. Rui, J. Jin, M. Wu, X. Wu, Z. Wen, *JOM* **2016**, *68*, 2593-2600.

- [12] X. Peng, K. Huang, S. Song, F. Wu, Y. Xiang, X. Zhang, *ChemElectroChem* **2020**, *7*, 2389–2394;
- [13] T. Jiang, P. He, G. Wang, Y. Shen, C. W. Nan, L. Z. Fan, *Adv. Energy Mater.* **2020**, *10*, 1903376.
- [14] Y. Tian, F. Ding, H. Zhong, C. Liu, Y.-B. He, J. Liu, X. Liu, Q. Xu, *Energy Storage Mater.* **2018**, *14*, 49–57.
- [15] J. Wolfenstine, J. L. Allen, J. Read, J. Sakamoto, *J. Mater. Sci.* **2013**, *48*, 5846–5851.
- [16] H.-S. Kim, J. B. Cook, H. Lin, J. S. Ko, S. H. Tolbert, V. Ozolins, B. Dunn, *Nat. Mater.* **2017**, *16*, 454–460.
- [17] a) Y. Zhou, Y. Liu, W. Wu, Y. Zhang, M. Gao, H. Pan, *J. Phys. Chem. C* **2012**, *116*, 1588–1595; b) P. Plerdsranoy, D. Kaewsuwan, N. Chanlek, R. Utke, *Int. J. Hydrogen Energy*, **2017**, *42*, 6189–6201.
- [18] K. Alexander, E. Tobschal, P. Heitjans, *Z. Phys. Chem.* **2009**, *223*, 1359–1377.
- [19] E. Deprez, M. A. Muñoz-Márquez, M. C. Jimenez de Haro, F. J. Palomares, F. Soria, M. Dornheim, R. Bormann, A. Fernández, *J. Appl. Phys.* **2011**, *109*, 014913.
- [20] D. A. Hensleyh, S. H. Garofalini, *Appl. Surface Sci.* **1994**, *81*, 331–339.
- [21] L. Cheng, E. J. Crumlin, W. Chen, R. Qiao, H. Hou, S. Franz Lux, V. Zorba, R. Russo, R. Kostecki, Z. Liu, K. Persson, W. Yang, J. Cabana, T. Richardson, G. Chen, M. Doeff, *Phys. Chem. Chem. Phys.* **2014**, *16*, 18294–18300.
- [22] a) Z. Lu, F. Ciucci, *Chem. Mater.* **2017**, *29*, 9308–9319; b) Y. M. Basalaev, E. S. Boldyreva, E. B. Duginova, *Russ. Phys. J.* **2019**, *61*, 1868–1875.
- [23] M. Matsuo, S. Orimo, *Adv. Energy Mater.* **2011**, *1*, 161–172
- [24] a) F. Mo, J. Ruan, S. Sun, Z. Lian, S. Yang, X. Yue, Y. Song, Y. N. Zhou, F. Fang, G. Sun, S. Peng, D. Sun, *Adv. Energy Mater.* **2019**, *9*, 1902123; b) K. Kisu, S. Kim, H. Oguchi, N. Toyama, S. Orimo, *J. Power Sources* **2019**, *436*, 226821.

- [25] S. Kumazaki, Y. Iriyama, K.-H. Kim, R. Murugan, K. Tanabe, K. Yamamoto, T. Hirayama, Z. Ogumi, *Electrochem. Commun.* **2011**, *13*, 509-512.
- [26] a) H. Buschmann, S. Berendts, B. Mogwitz, J. Janek, *J. Power Sources* **2012**, *206*, 236-244; b) K. Tadanaga, R. Takano, T. Ichinose, S. Mori, A. Hayashi, M. Tatsumisago, *Electrochem. Commun.* **2013**, *33*, 51-54.
- [27] A. Mei, X. Wang, Y. Feng, S. Zhao, G. Li, H. Geng, Y. Lin, C. Nan, *Solid State Ionics* **2008**, *179*, 2255-2259.
- [28] a) Y. Li, Y. Cao, X. Guo, *Solid State Ionics* **2013**, *253*, 76-80; b) F. Han, A. S. Westover, J. Yue, X. Fan, F. Wang, M. Chi, D. N. Leonard, N. J. Dudney, H. Wang, C. Wang, *Nat. Energy* **2019**, *4*, 187-196.
- [29] T. Deng, X. Ji, Y. Zhao, L. Cao, S. Li, S. Hwang, C. Luo, P. Wang, H. Jia, X. Fan, X. Lu, D. Su, X. Sun, C. Wang, J. G. Zhang, *Adv. Mater.* **2020**, *32*, 2000030.
- [30] H. Liu, Z. Ren, X. Zhang, J. Hu, M. Gao, H. Pan, Y. Liu, *Chem. Mater.* **2020**, *32*, 671-678.

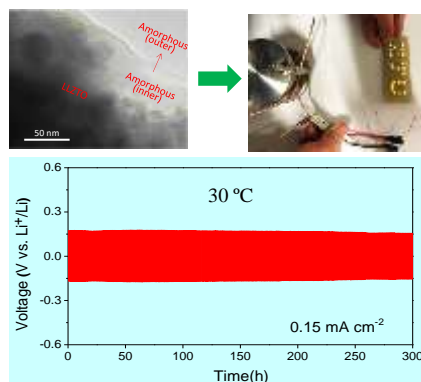
**A unique amorphous dual layer-coated LLZTO composite** with  $\text{LiBO}_2$  as the inner layer and  $\text{LiBH}_4$  as the outer layer was successfully fabricated by a facile mechanochemical process. This novel non-sintered composite electrolyte features high Li-ion conductivity and high Li transference number, and enables long-term cyclability of symmetric Li-Li cells at ambient temperature.

**Keywords:** energy storage materials, rechargeable Li batteries, solid state electrolyte, borohydrides, LLZTO

*Yuan Gao, Shuyang Sun, Xin Zhang, Yongfeng Liu\*, Jianjiang Hu, Zhenguo Huang, Mingxia Gao, and Hongge Pan*

### **Amorphous Dual-layer Coating: Enabling High Li-ion Conductivity of Non-sintered Garnet-type Solid Electrolyte**

#### **ToC figure**



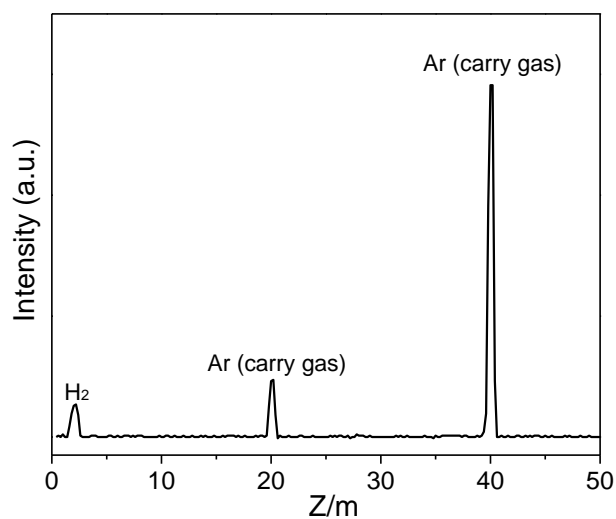
## Supporting Information

**Amorphous Dual-layer Coating: Enabling High Li-ion Conductivity of Non-sintered Garnet-type Solid Electrolyte**

*Yuan Gao, Shuyang Sun, Xin Zhang, Yongfeng Liu\*, Jianjiang Hu, Zhenguo Huang, Mingxia Gao, and Hongge Pan*

**Table S1.** Ionic conductivity and  $E_a$  values of the LLZTO- $x$ LiBH<sub>4</sub> samples.

Samples	$\sigma_{\text{Li}^+}$ (S cm <sup>-1</sup> )	$E_a$ (eV)
Pristine LLZTO	$4.17 \times 10^{-9}$	0.70
LLZTO-2LiBH <sub>4</sub>	$3.94 \times 10^{-6}$	0.67
LLZTO-4LiBH <sub>4</sub>	$8.02 \times 10^{-5}$	0.60
LLZTO-6LiBH <sub>4</sub>	$1.12 \times 10^{-5}$	0.62
LLZTO-8LiBH <sub>4</sub>	$9.42 \times 10^{-6}$	0.63

**Figure S1.** MS signal of gaseous products obtained from the mechanochemical reaction between LLZTO and LiBH<sub>4</sub>.

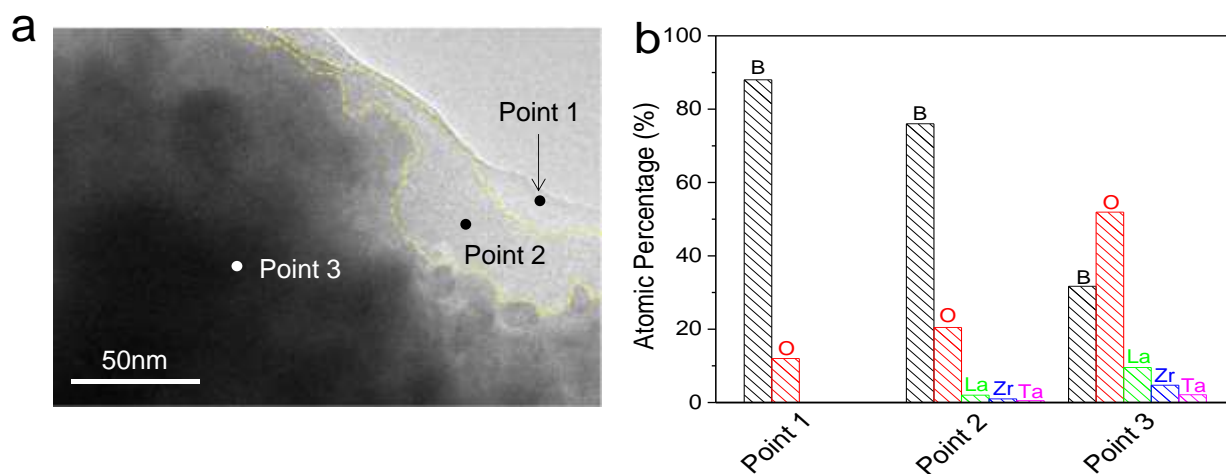


**Figure S2.** TEM image of the LLZTO-4LiBH<sub>4</sub> sample (a) and corresponding atomic compositions of point 1, 2 and 3 (b).

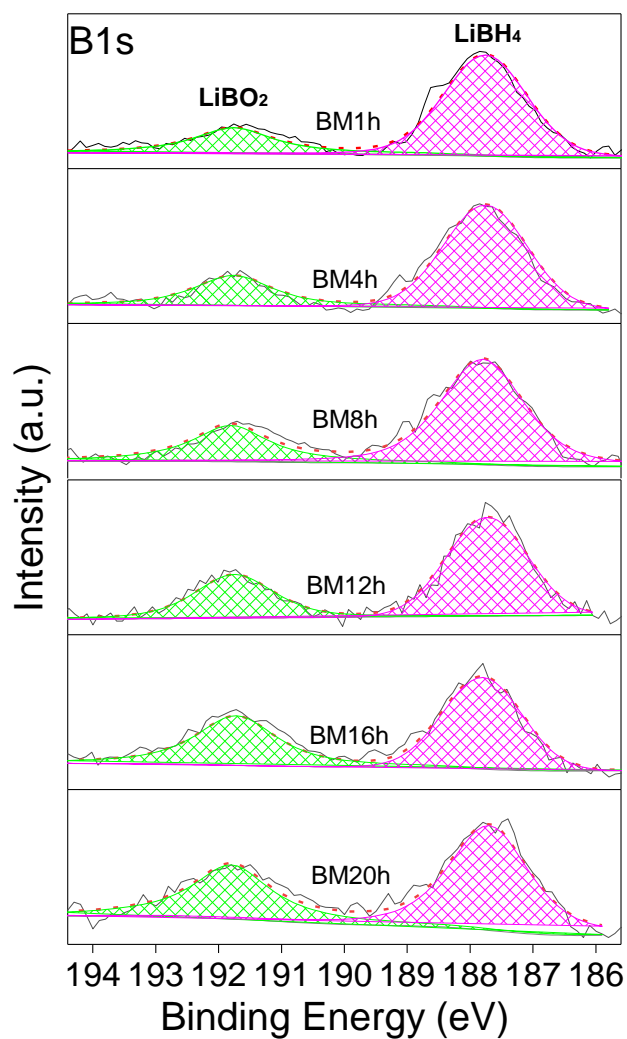


**Figure S3.** High resolution XPS spectra of B 1s of the LLZTO-4LiBH<sub>4</sub> sample ball milled for different times.

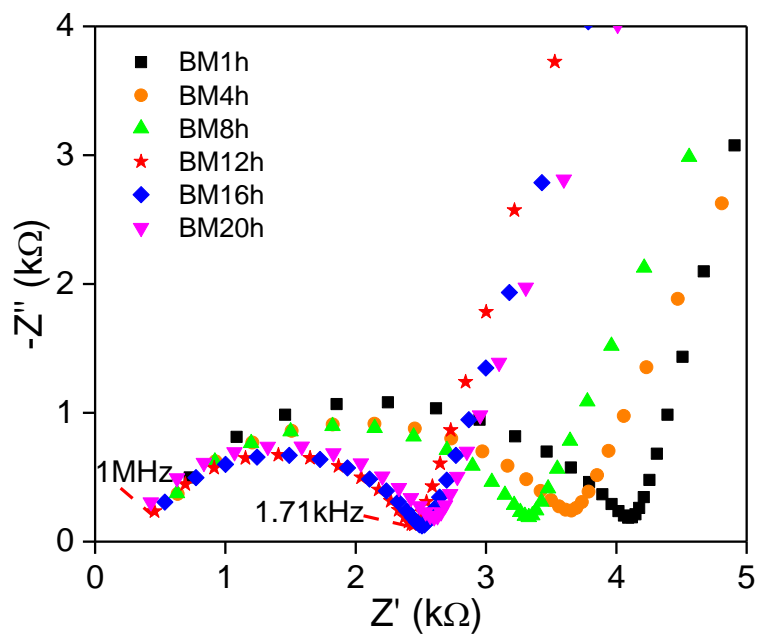


**Figure S4.** EIS curves of the LLZTO-4LiBH<sub>4</sub> sample ball milled for different times.

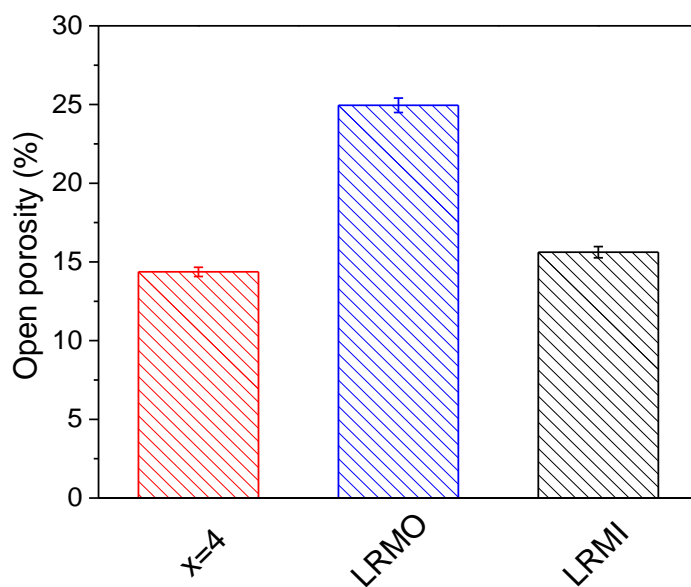


**Figure S5.** Open porosity of the LLZTO-4LiBH<sub>4</sub> sample after different treatments.

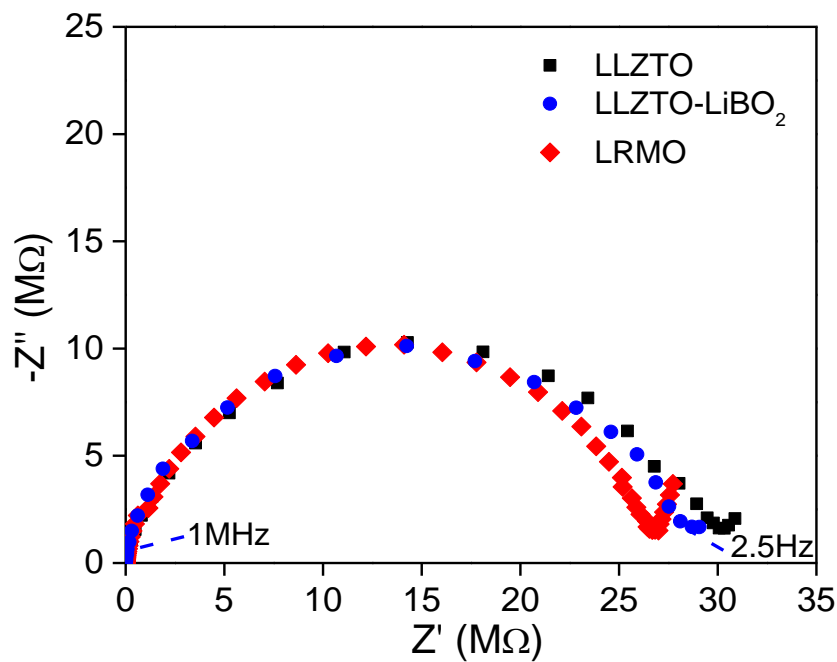


**Figure S6.** EIS curves of LLZTO, LLZTO-LiBO<sub>2</sub> and LMRO samples.

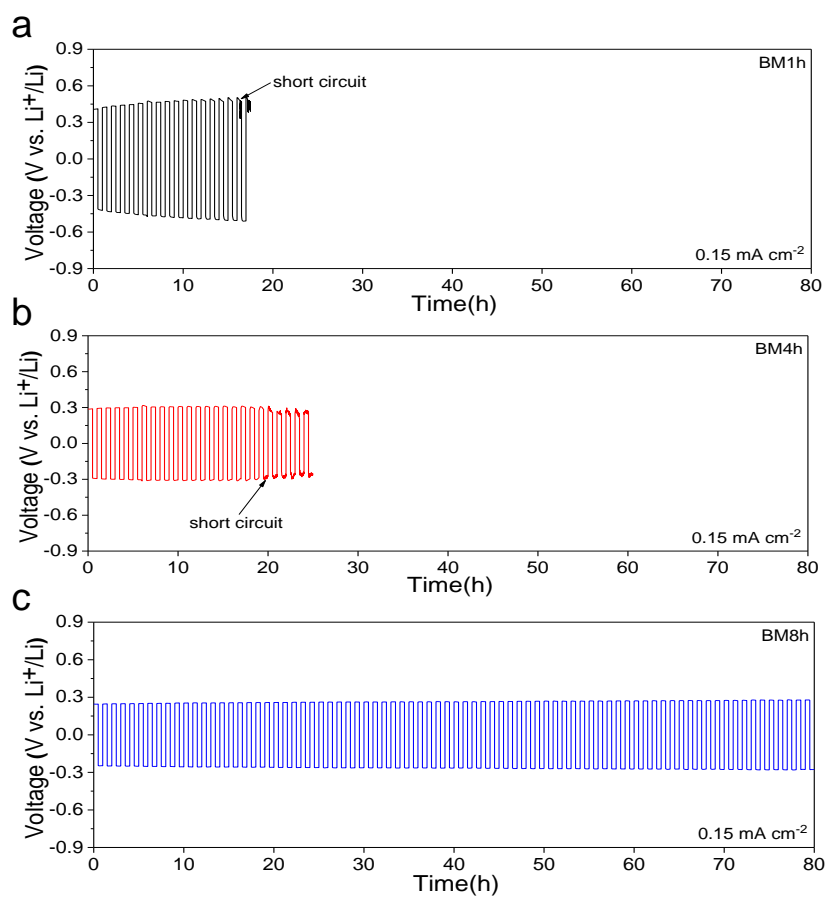


**Figure S7.** Galvanostatic cycling curves of the Li symmetric cells with LLZTO-4LiBH<sub>4</sub> ball milled for different times.